Global CO_2 Distributions over Land from the Greenhouse Gases Observing Satellite (GOSAT)

Dorit M. Hammerling[a], Anna M. Michalak[a,b], Christopher O'Dell[c] and S. Randolph Kawa[d]

[a] Department of Civil and Environmental Engineering, University of Michigan, MI, USA

[b] Department of Global Ecology, Carnegie Institution for Science, Stanford, CA, USA

[c] Department of Atmospheric Science, Colorado State University, Fort Collins, CO, USA

[d] NASA Goddard Space Flight Center, Greenbelt, MD, USA

Abstract

January 2009 saw the successful launch of the first space-based mission specifically designed for measuring greenhouse gases, the Japanese Greenhouse gases Observing SATellite (GOSAT). We present global land maps (Level 3 data) of column-averaged CO_2 concentrations (X_{CO2}) derived using observations from the GOSAT ACOS retrieval algorithm, for July through December 2009. The applied geostatistical mapping approach makes it possible to generate maps at high spatial and temporal resolutions that include uncertainty measures and that are derived directly from the Level 2 observations, without invoking an atmospheric transport model or estimates of CO_2 uptake and emissions. As such, they are particularly well suited for comparison studies. Results show that the Level 3 maps for July to December 2009 on a $1^\circ \times 1.25^\circ$ grid, at six-day resolution capture much of the synoptic scale and regional variability of X_{CO2}, in addition to its overall seasonality. The uncertainty estimates, which reflect local data coverage, X_{CO2} variability, and retrieval errors, indicate that the Southern latitudes are relatively well-constrained, while the Sahara Desert and the high Northern latitudes are weakly-constrained. A probabilistic comparison to the PCTM/GEOS-5/CASA-GFED model reveals that

the most statistically significant discrepancies occur in South America in July and August, and central Asia in September to December. While still preliminary, these results illustrate the usefulness of a high spatiotemporal resolution, data-driven Level 3 data product for direct interpretation and comparison of satellite observations of highly dynamic parameters such as atmospheric CO_2.

1 Introduction

The Greenhouse gases Observing SATellite "Ibuki" (GOSAT) launched on January 23, 2009, and is the first space-based mission to reach orbit that was designed specifically for making high-precision measurements of carbon dioxide (CO_2) and methane (CH_4) with sensitivity in the lower troposphere [Kuze et al. 2009; Yokota et al. 2009]. After the launch failure of the Orbiting Carbon Observatory (OCO) mission (e.g. Crisp et al. 2004), the OCO team was invited to join the GOSAT team in analyzing GOSAT observations, under the auspices of the NASA Atmospheric CO_2 Observations from Space (ACOS) task. The ACOS GOSAT column CO_2 (X_{CO2}) retrieval algorithm has now reached a level of maturity that makes it possible to use its estimates for informing carbon cycle science [O'Dell et al. 2012; Crisp et al. 2012]. Version 2.9 of the Level 2 data product, which represents geo-referenced X_{CO2} observations, includes approximately 900 successful retrievals per three-day repeat cycle during the second half of 2009, the first period for which data are available. The majority of these observations are over land.

Although these data are useful in their own right, they have large gaps (e.g. Figure 1a and Figure A1 in the auxiliary materials) and substantial retrieval uncertainties [O'Dell et al. 2012], which makes it difficult to interpret their scientific significance without further analysis.

Hammerling et al. [2012] recently developed a statistical mapping approach that makes it possible to create full-coverage (i.e. Level 3) maps from satellite X_{CO2} observations at high spatial and temporal resolutions. Unlike commonly used spatial and temporal binning and averaging procedures (e.g., Crevoisier et al. [2009]; Kulawik et al. [2010]; Tiwari et al. [2006]), this approach exploits the spatial correlation among the Level 2 observations and the resulting Level 3 product describes the X_{CO2} concentrations as a stochastic field characterized by its mean ("Level 3 estimates") and variance ("Level 3 uncertainties") structure.

Furthermore, unlike maps derived from inverse modeling or data assimilation studies (e.g. Engelen et al. [2009]), the Hammerling et al. [2012] approach draws information about the degree of spatial variability of X_{CO2} directly from the X_{CO2} observations, without additional information introduced from an atmospheric transport model or CO_2 flux estimates. As such, because no information from atmospheric transport models or CO_2 flux estimates is incorporated, the resulting Level 3 maps are a more direct representation of the information content of the retrievals. Rather than being intended as inputs to inverse modeling studies, these Level 3 X_{CO2} products enable direct independent comparisons with existing models of carbon flux and atmospheric transport. The uncertainty measures provided by the approach make it possible to conduct these comparisons in a probabilistic framework.

This paper presents global Level 3 X_{CO2} products over land derived from the GOSAT ACOS X_{CO2} retrievals, covering the second half of 2009. The Level 3 estimates and their associated uncertainties are compared to predictions for the same period from a combined CO_2 flux and atmospheric transport model using a probabilistic framework.

2 Data and Methods

2.1 GOSAT ACOS X_{CO2} Level 2 data

GOSAT flies in a sun-synchronous orbit with an approximate 1pm equator-crossing time and has a three-day repeat-cycle. Version 2.9 of the GOSAT ACOS X_{CO2} Level 2 data product is used in this study; only high (H) gain data were used as recommended in Crisp et al. [2012]. Figure 1a shows an example of six days (i.e. two repeat cycles) of ACOS L2 data for August 2009.

2.2 Method for creating global GOSAT ACOS X_{CO2} Level 3 maps

The geostatistical methodology applied for creating Level 3 maps exploits the spatial correlation of the X_{CO2} observations and consists of two major steps. In the first step, the spatial covariance structure of the X_{CO2} observations is inferred from these observations. In the second step, the inferred spatial covariance structure and the observations are used to estimate the X_{CO2} field. The approach is described in detail by Hammerling et al. [2012], and only key implementation details are presented here. Due to the currently limited availability of GOSAT ACOS X_{CO2} observations over the oceans, the estimation has been restricted to land areas. The mapping is implemented on a 1° latitude × 1.25° longitude grid, to inform regional variability and to correspond with that of the model used for comparison in Section 4.

Based on previous work [Alkhaled et al., 2008], an exponential covariance function is used to represent the X_{CO2} spatial correlation:

$$C(h) = \sigma^2 exp\left(-\frac{h}{l}\right), \quad (1)$$

where the covariance C is a function of the separation distance between locations (h), and spatially-variable variance (σ^2) and range (l) parameters that are inferred at each estimation location from the Level 2 data.

A local kriging procedure is then applied to create full-coverage maps, using a weighted average of available observations by solving the following linear system of equations once for each location on the Level 3 map:

$$\begin{bmatrix} \mathbf{Q}+\mathbf{R} & \mathbf{1} \\ \mathbf{1}^T & 0 \end{bmatrix} \begin{bmatrix} \boldsymbol{\lambda} \\ v \end{bmatrix} = \begin{bmatrix} \boldsymbol{q} \\ 1 \end{bmatrix}, \tag{2}$$

where $\mathbf{Q}$ is an $n \times n$ covariance matrix among the n observation locations, as defined in eq. 1, $\mathbf{R}$ is an $n \times n$ diagonal matrix with the retrieval error variance specific to each observation on the diagonal, $\boldsymbol{\lambda}$ is a $n \times 1$ vector of weights, v is a Lagrange multiplier and $\boldsymbol{q}$ is the $n \times 1$ vector of the spatial covariances between an individual estimation location and the observation locations, also defined using eq. 1. In this study, the measurement error variances are the squares of the reported ACOS Level 2 measurement error standard deviations adjusted by a factor of 2.1 as derived by O'Dell et al. [2012]. The predicted X_{CO2} value, $\hat{y}$, and the prediction uncertainty, $\sigma^2_{\hat{y}}$, at each Level 3 location are:

$$\hat{y} = \boldsymbol{\lambda}^T \mathbf{y} \tag{3}$$

$$\sigma^2_{\hat{y}} = \sigma^2 - \boldsymbol{\lambda}^T \boldsymbol{q} - v, \tag{4}$$

where $\mathbf{y}$ are the observations at the n Level 2 locations and σ^2 is the variance as shown in eq 1.

Based on previous work, a 2000 km neighborhood is required for assessing the local spatial variability (eq. 1, also see Hammerling et al. [2012] for details), and estimates can therefore only be obtained if there is a minimum of three observations within this distance of each estimation location. Estimation locations not meeting this requirement are shown as white

in Figures 1b and A2. It is the uncertainties in eq. 4, however, that should be used as the criterion for limiting the coverage of Level 3 maps to regions where they are interpretable for a given scientific application (e.g. Figure 2), and one of the advantages of the method is the flexibility to dynamically define this uncertainty tolerance.

2.3 PCTM/GEOS-5/CASA-GFED model data

The modeled X_{CO2} data used in the intercomparison are based on the Goddard Space Flight Center parameterized chemistry and transport model, which is driven by real-time analyzed meteorological fields from the Goddard Global Modeling and Assimilation Office, version GEOS-5, and uses biospheric fluxes produced from the Carnegie-Ames-Stanford-Approach, which incorporate biomass burning from the Global Fire Emissions Database (PCTM/GEOS-5/CASA-GFED), as well as oceanic, and anthropogenic CO_2 flux estimates, as described by Kawa et al. [2004; 2010]. The model resolution is $1° \times 1.25°$ with 28 vertical levels and hourly output. CO_2 mixing ratios were pressure-averaged to simulate the vertical sensitivity of the GOSAT observations. The PCTM/GEOS-5/CASA-GFED model has been widely tested, and has shown favorable results in carbon cycle comparison studies (e.g. Kawa et al. [2010] and references therein).

3 ACOS GOSAT X_{CO2} Level 3 maps

The choice of the temporal resolution, meaning the time period over which observations are aggregated, is an important decision in the creation of a Level 3 product [Hammerling et al., 2012]. Ideally Level 3 products are created for the shortest time period possible to preserve as much of the short-term dynamical information as possible. However, this needs to be balanced with a minimum requirement for spatial coverage by the GOSAT observations. Based on initial investigations of temporal resolutions ranging from three days to one month, a resolution of six-

days fulfilled both these objectives for all 30 six-day periods investigated from July to December 2009.

Figure 1 provides an example of one of the investigated periods, August 7-12 2009. The Level 3 map (Figure 1b) for this period shows comparatively low X_{CO2} in the Northern latitudes consistent with the knowledge of the effect of the seasonal cycle on CO_2 concentrations. The fact that the seasonal cycle in the Northern hemisphere is captured well in the GOSAT ACOS Level 3 maps becomes further evident from results from the full examined period (see Figure A2 in auxiliary materials), which show a pronounced increase in CO_2 concentrations in the Northern latitudes in the winter months as well as a more subtle increase in the overall CO_2 concentrations. The comparatively high X_{CO2} over South America visible in the Level 3 map for August 7-12 (Figure 1b) are a fairly persistent feature throughout the summer months (figure A2) and are further discussed in Section 4.

An advantage of the mapping method used in this study is that each estimate has an associated uncertainty measure (Figure 1c), which reflects the number of observations surrounding an estimation location, their retrieval errors, and the spatial variability in the X_{CO2} field. Locations where the prediction uncertainties are below specific cut-off values are illustrated in Figure 2. For this six-day period, the predictions uncertainties are low for Australia, the southern part of Africa and eastern South America, whereas they are high for Southeast Asia, parts of India and the eastern United States and Canada. Analyzing these prediction uncertainties over extended time periods highlights the degree to which ACOS GOSAT retrievals constrain the X_{CO2} distribution for different regions. Figure 3 summarizes this analysis for the 30 investigated six-day periods in 2009, identifying Australia, Southern Africa and a region in South America covering approximately eastern Brazil, Paraguay, Uruguay and

central and northern Argentina and northern Chile as well-observed regions. Regions with the weakest constraint are the Sahara Desert and the high Northern Latitudes including Alaska, northern Canada, Greenland, Scandinavia and northern Russia.

The interplay of how the number of observations, their retrieval errors, and the spatial variability in the X_{CO2} field contribute to the uncertainty at each location renders it difficult to completely separate the effect of these contributing factors. The spatial coverage over the larger land masses in the Southern hemisphere, namely Australia, southern Africa and southern South America, is generally good. The number of observations decreases somewhat towards the end of the year, but these observations have lower retrieval errors and are supplemented by nearby ocean observations, which shift southwards in the second half of year as a function of the solar zenith angle. Southeast Asia and central and eastern China, on the other hand, have very poor coverage during July to October due to persistent cloudiness, but notably better coverage in November and December, leading to the mapping uncertainties being seasonally variable. The United States have generally good coverage, but the X_{CO2} spatial variability over the Northern hemisphere land masses is rather high, yielding somewhat higher uncertainties for North America than for areas with comparable spatial coverage but less spatial variability such as Australia. There are no observations over the Sahara Desert, due to our exclusion of the GOSAT M-gain data (see Crisp et al. [2012] for details). The high Northern latitudes lack observations in November and December due to solar zenith angle restrictions; and the observations in July to October have comparatively high retrieval errors. This, coupled with the high X_{CO2} spatial variability in the high Northern latitudes, leads to high mapping uncertainties even when data are present.

4 Comparison of Level 3 maps to modeled X_{CO2}

The ACOS GOSAT X_{CO2} Level 3 products can be used to conduct intercomparisons with models, by using the Level 3 data and their associated uncertainties to probabilistically identify areas where model outputs differ significantly from the Level 3 maps.

Figure 4 shows an example of such an intercomparison to the PCTM/GEOS-5/CASA-GFED model for August 7-12 2009. The difference plot (Figure 4b) shows large differences in North America, the Amazon Region, and in a region covering the Northeastern part of India and Bangladesh. The standardized differences (Figure 4c), on the other hand, incorporate the Level 3 uncertainties, and can therefore be used to assess the significance of these differences given the information content of the satellite observations. For example, while the difference in North America and Southeast Asia might appear large in Figure 4b, they are not highly significant, as shown in Figure 4c. This is due to the comparatively large Level 3 uncertainties in these regions for this period.

Figure 5 summarizes the intercomparison for July to December 2009, and reveals that discrepancies are most pronounced over South America for the Northern hemisphere summer months and shift to Asia in the Northern hemisphere fall. Although these results likely point to areas where the PCTM/GEOS-5/CASA-GFED model flux and transport processes need to be re-examined, Level 2 retrieval biases and, in the case of the sparsely-sampled Amazon region, underestimation of the Level 3 uncertainties due to low X_{CO2} variability in surrounding well-sampled regions cannot be absolutely eliminated at this stage. It is also interesting to note that certain regions exhibit few or no limited significant differences over the entire examined period, including the high Northern latitudes, North America, Northern Africa, the Arabian Peninsula and Australia. The conclusion one can draw from an absence of statistically significant

discrepancies depends on how well constrained a region is. For example, the high Northern latitudes are weakly constrained and have high mapping uncertainties. This implies that even large discrepancies are not conclusive because the power to detect a difference is low for that region. For Australia, on the other hand, the Level 3 uncertainties are rather low, so an absence of detectable discrepancies indicates that the Level 3 maps are indeed consistent with the model outputs.

5 Conclusions

This paper presents global X_{CO2} Level 3 products over land based on the ACOS GOSAT X_{CO2} data. The implemented approach (Hammerling et al., 2012) yields maps at high spatial and temporal resolutions, using information derived directly from the Level 2 observations, without invoking an atmospheric transport model or estimates of CO_2 uptake and emissions. One limitation of such a purely observation-driven approach is that local enhancement phenomena that are not observed by the satellite cannot be fully captured. This results in Level 3 maps with smoother features than expected in the real X_{CO2} concentration fields, but with uncertainty bounds that are wide enough to capture the range of likely variability.

Level 3 maps for July to December 2009 at six-day resolution capture much of the synoptic scale and regional variability of X_{CO2}, in addition to the overall seasonality. Results include robust uncertainty estimates, which reflect local data coverage, X_{CO2} variability, and retrieval errors. Uncertainties are generally highest in the northern hemisphere in July and August, during the height of the growing season (Figure A3), and lowest in areas with good data coverage and low CO_2 variability in the Southern Hemisphere (Figure A3).

A probabilistic comparison to a state of the art model reveals that the most significant discrepancies captured by the ACOS GOSAT Level 3 maps are in the South America in July and

August, and central Asia in September to December (Figure 5). The differences in South America are significant in part because the Level 3 uncertainties are low in this region, and may reveal inaccuracies in carbon flux estimates for this region that is poorly constrained by in situ atmospheric CO_2 observations, although problems with the Level 2 retrievals and with identifying local phenomena in the Amazon region in the Level 3 products cannot be ruled out at this stage. Similarly, the significant differences in Asia appear during months when the Level 3 mapping uncertainties are lowest in this region (Figure A3).

These early results illustrate the usefulness of a high spatiotemporal resolution, data-driven Level 3 data product with uncertainty measures. Such a Level 3 data product can be used for direct interpretation of satellite observations, including those of highly dynamic parameters such as atmospheric CO_2, and for probabilistic comparison studies.

Acknowledgements

This material is based upon work supported by the National Aeronautics and Space Administration under Grant NNX08AJ92G issued through the Research Opportunities in Space and Earth Sciences (ROSES) Carbon Cycle Science program. We are grateful to the ACOS and GOSAT teams for the availability of GOSAT observations and thank various members of these teams for their helpful contributions to this study.

References

Alkhaled, A., A. M. Michalak, S. R. Kawa, S. Olsen, and J. Wang (2008), A global evaluation of the regional spatial variability of column integrated CO_2 distributions, *J.Geophys.Res., 113*(d20), D20303, doi: 10.1029/2007JD009693.

Crevoisier, C., A. Chédin, H. Matsueda, T. Machida, R. Armante, and N. A. Scott (2009), First year of upper tropospheric integrated content of CO2 from IASI hyperspectral infrared observations *Atmos. Chem. Phys., 9*(14), 4797-4810.

Crisp, D., R. M. Atlas, F. Bréon, L. R. Brown, J. P. Burrows, P. Ciais, B. J. Connor, S. C. Doney, I. Y. Fung, D. J. Jacob, C. E. Miller, D. M. O'Brien, S. Pawson, J. T. Randerson, P. J. Rayner, R. J. Salawitch, S. P. Sander, B. Sen, G. L. Stephens, P. P. Tans, G. C. Toon, P. O. Wennberg, S. C. Wofsy, Y. L. Yung, Z. Kuang, B. Chudasama, G. Sprague, B. Weiss, R. Pollock, D. Kenyon, and S. Schroll (2004), The Orbiting Carbon Observatory (OCO) mission *Advances in Space Research, 34*(4), 700-709, doi:DOI: 10.1016/j.asr.2003.08.062.

Crisp, D., Fisher, B. M., O'Dell, C., Frankenberg, C., Basilio, R., Bösch, H., Brown, L. R., Castano, R., Connor, B., Deutscher, N. M., Eldering, A., Griffith, D., Gunson, M., Kuze, A., Mandrake, L., McDuffie, J., Messerschmidt, J., Miller, C. E., Morino, I., Natraj, V., Notholt, J., O'Brien, D., Oyafuso, F., Polonsky, I., Robinson, J., Salawitch, R., Sherlock, V., Smyth, M., Suto, H., Taylor, T., Thompson, D. R., Wennberg, P. O., Wunch, D., and Yung, Y. L.(2012), The ACOS X_{CO2} retrieval algorithm, Part 2: Global X_{CO2} data characterization, Atmos. Meas. Tech. Discuss., 5, 1-60, doi:10.5194/amtd-5-1-2012

Engelen, R. J., S. Serrar, and F. Chevallier (2009), Four-dimensional data assimilation of atmospheric CO_2 using AIRS observations, *J.Geophys.Res., 114*(d3), D03303, doi: 10.1029/2008JD010739.

Hammerling, D. M., A. M. Michalak, and S. R. Kawa (2012, *in press*), Mapping of CO_2 at High Spatiotemporal Resolution using Satellite Observations: Global Distributions from OCO-2, *J. Geophys. Res.*, doi:10.1029/2011JD017015.

Kawa, S. R., D. J. Erickson III, S. Pawson, and Z. Zhu (2004), Global CO_2 transport simulations using meteorological data from the NASA data assimilation system, *J.Geophys.Res., 109*, doi: 10.1029/2004JD004554.

Kawa, S. R., J. Mao, J. B. Abshire, G. J. Collatz, X. Sun, and C. J. Weaver (2010), Simulation studies for a space-based CO_2 lidar mission, *Tellus B, 62*(5), 759-769, doi: 10.1111/j.1600-0889.2010.00486.x.

Kulawik, S. S., D. B. A. Jones, R. Nassar, F. W. Irion, J. R. Worden, K. W. Bowman, T. Machida, H. Matsueda, Y. Sawa, S. C. Biraud, M. L. Fischer, and A. R. Jacobson (2010), Characterization of Tropospheric Emission Spectrometer (TES) CO_2 for carbon cycle science *Atmospheric Chemistry and Physics, 10*(12), 5601-5623.

Kuze, A., H. Suto, M. Nakajima, and T. Hamazaki (2009), Thermal and near infrared sensor for carbon observation Fourier-transform spectrometer on the Greenhouse Gases Observing Satellite for greenhouse gases monitoring, *Appl.Opt., 48*, 6716-6733, doi:10.1364/AO.48.006716.

O'Dell, C. W., B. Connor, H. Bösch, D. O'Brien, C. Frankenberg, R. Castano, M. Christi, D. Crisp, A. Eldering, B. Fisher, M. Gunson, J. McDuffie, C. E. Miller, V. Natraj, F. Oyafuso, I. Polonsky, M. Smyth, T. Taylor, G. C. Toon, P. O. Wennberg, and D. Wunch (2012), The ACOS CO_2 retrieval algorithm - Part 1: Description and validation against synthetic observations, *Atmos. Meas. Tech.*, 5, 99-121, doi:10.5194/amt-5-99-2012.

Yokota, T., Y. Yoshida, N. Eguchi, Y. Ota, T. Tanaka, H. Watanabe, and S. Maksyutov (2009), Global Concentrations of CO_2 and CH_4 Retrieved from GOSAT: First Preliminary Results *SOLA, 5*, 160-163, doi:10.2151/sola.2009-041.

Tiwari, Y. K., M. Gloor, R. J. Engelen, F. Chevallier, C. Rödenbeck, S. Körner, P. Peylin, B. H. Braswell, and M. Heimann (2006), Comparing CO2 retrieved from Atmospheric Infrared

Sounder with model predictions: Implications for constraining surface fluxes and lower-to-upper troposphere transport *J. Geophys. Res., 111*, D17106, doi:10.1029/2005JD006681.

Figure Captions

Figure 1: ACOS X_{CO2} Level 2 data ("Observations"), ACOS X_{CO2} Level 3 product ("Estimates") and estimated prediction uncertainties ("Uncertainty") expressed as a standard deviation for August 7-12 2009.

Figure 2: ACOS Level 3 X_{CO2} map for August 7-12 (Figure 1b) filtered for locations where the standard deviations of the prediction uncertainties (Figure 1c) are less than 2.5ppm, less than 2ppm and less than 1ppm, respectively.

Figure 3: Summary of the analysis of prediction uncertainties from 30 6-day periods from July through December 2009. For each location, the number of 6-day prediction periods with prediction uncertainties below 2.5 ppm, 1.5 ppm and 1 ppm, respectively, is shown. Lighter colors indicated regions which are better constrained by the GOSAT observations.

Figure 4: PCTM model predictions for the same 6-day period as shown in Figure 1, difference and discretized standardized difference between the ACOS Level 3 map and the PCTM model. In the difference plot, values in the copper range indicate areas where the ACOS Level 3 values exceed the PCTM model predictions, values in the blue range areas where the PCTM model exceed the ACOS Level 3 values. The standardized difference is the absolute difference divided by the standard deviation of the prediction uncertainty at each location. The values are discretized to improve the visualization. Areas in yellow represent differences larger than one standard deviation of the prediction uncertainty, areas in orange larger than two standard deviations and areas in dark red larger than three standard deviations. The PCTM data

has been mean-adjusted to the ACOS Level 3 predictions so that the global spatial average of the PCTM data and the ACOS Level 3 is equal.

Figure 5: Percentage of 6-day periods within each month where the standardized differences exceed two prediction uncertainties. Given that there are only five 6-day periods in each month, we have chosen a discretized color scale to visualize percentages.

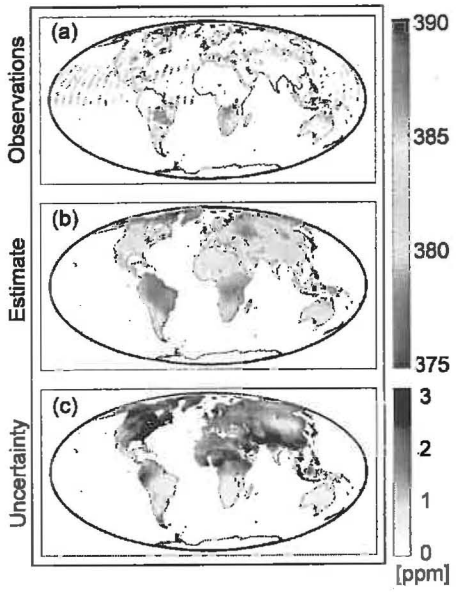
(a)
(b)
(c)
Observations
Estimate
Uncertainty
390
385
380
375
3
2
1
0
[ppm]

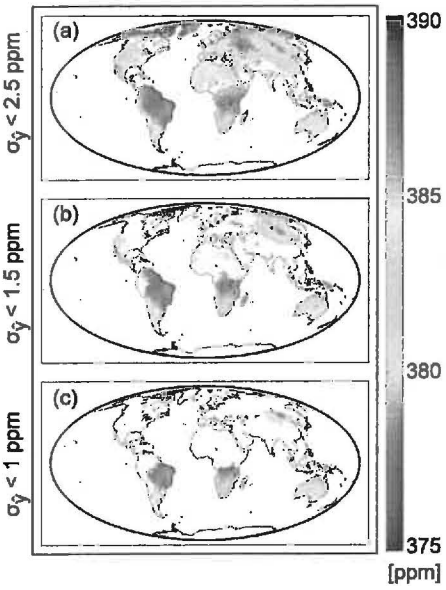
(a)
(b)
(c)
$\sigma_{\hat{y}} < 2.5$ ppm
$\sigma_{\hat{y}} < 1.5$ ppm
$\sigma_{\hat{y}} < 1$ ppm
390
385
380
375
[ppm]

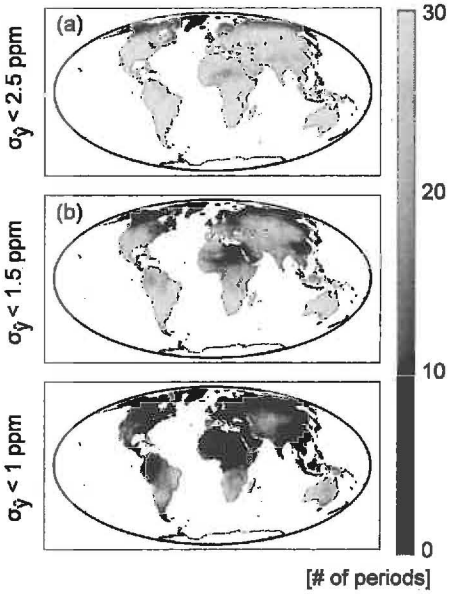
(a)
(b)
σ_y < 2.5 ppm
σ_y < 1.5 ppm
σ_y < 1 ppm
30
20
10
0
[# of periods]

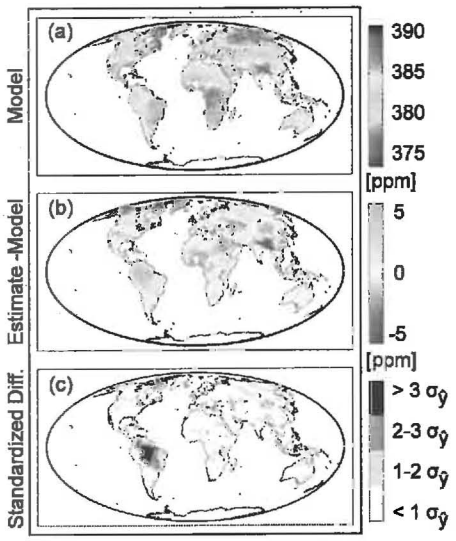
(a)
(b)
(c)
Model
Estimate -Model
Standardized Diff.
390
385
380
375
[ppm]
5
0
-5
[ppm]
> 3 σŷ
2-3 σŷ
1-2 σŷ
< 1 σŷ

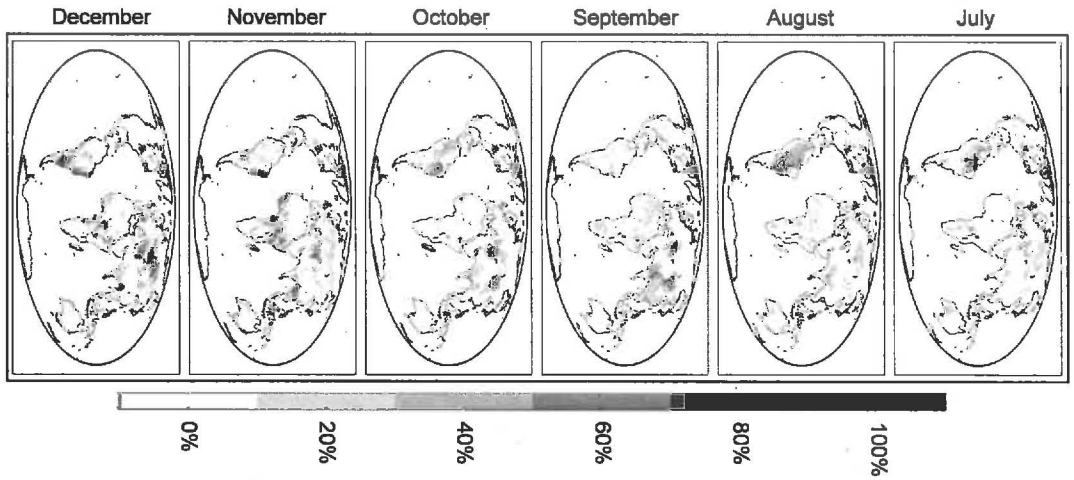
December
November
October
September
August
July
0%
20%
40%
60%
80%
100%